HHS Public Access

Author manuscript

J Am Chem Soc. Author manuscript; available in PMC 2015 July 17.

Published in final edited form as:

J Am Chem Soc. 2011 June 8; 133(22): 8586–8593. doi:10.1021/ja1117446.

A Multistage Pathway for Human Prion Protein Aggregation in Vitro: From Multimeric Seeds to β-Oligomers and Nonfibrillar Structures

Kang R. Cho[†,‡], **Yu Huang**[‡], **Shuiliang Yu**[§], **Shaoman Yin**[§], **Marco Plomp**[†], **S. Roger Qiu**[†], **Rajamani Lakshminarayanan**[‖,#], **Janet Moradian-Oldak**[‖], **Man-Sun Sy**[§], and **James J. De Yoreo**[†,⊥]

Yu Huang: yhuang@seas.ucla.edu; James J. De Yoreo: jjdeyoreo@lbl.gov

[†]Physical and Life Sciences Directorate, Lawrence Livermore National Laboratory, Livermore, California 94550, United States

[‡]Department of Materials Science and Engineering, University of California, Los Angeles, Los Angeles, California 90095, United States

[§]Department of Pathology, Case Western Reserve University, Cleveland, Ohio 44106, United States

[‖]Center for Craniofacial Molecular Biology, Herman Ostrow School of Dentistry, University of Southern California, Los Angeles, California 90033, United States

[⊥]Molecular Foundry, Lawrence Berkeley National Laboratory, Berkeley, California 94720, United States

Abstract

Aberrant protein aggregation causes numerous neurological diseases including Creutzfeldt—Jakob disease (CJD), but the aggregation mechanisms remain poorly understood. Here, we report AFM results on the formation pathways of β-oligomers and nonfibrillar aggregates from wild-type full-length recombinant human prion protein (WT) and an insertion mutant (10OR) with five additional octapeptide repeats linked to familial CJD. Upon partial denaturing, seeds consisting of 3–4 monomers quickly appeared. Oligomers of ∼11–12 monomers then formed through direct interaction of seeds, rather than by subsequent monomer attachment. All larger aggregates formed through association of these β-oligomers. Although both WT and 10OR exhibited identical aggregation mechanisms, the latter oligomerized faster due to lower solubility and, hence, thermodynamic stability. This novel aggregation pathway has implications for prion diseases as well as others caused by protein aggregation.

Correspondence to: Yu Huang, yhuang@seas.ucla.edu; James J. De Yoreo, jjdeyoreo@lbl.gov.

[#]**Present Addresses**: Singapore Eye Research Institute, 7 Hospital Drive, Block C, 02-02, Singapore 169611.

Supporting Information. Supporting figures (Figures S1–S10) and complete ref 2. This material is available free of charge via the Internet at http://pubs.acs.org.

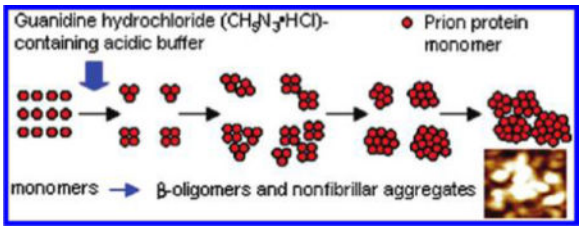

INTRODUCTION

Misfolding and aggregation of cellular proteins is thought to play a critical role in a number of human neurodegenerative diseases, such as Alzheimer's,[1] Parkinson's,[2] and prion diseases.[3–5] Among these, prion diseases are unique because they appear to share a common pathogenic mechanism based on the conversion of the normal α-helix-rich cellular prion protein (PrP^C) into the infectious and pathogenic *β*-sheet-rich scrapie prion protein (PrP^{Sc}).[6] An essential step in the conversion process is oligomerization of PrP^C into PrP^{Sc}. In vivo, PrP^{Sc} appears as aggregates of diffuse deposits or plaques.[7] In vitro, it forms amorphous aggregates,[6] amyloid fibril-like structures,[8] or two-dimensional crystals.[9] Although many studies of prion diseases, as well as other neuro-degenerative diseases, have focused on amyloid fibril formation, in humans, this structure is only observed in a small number of inherited forms of prion diseases. Moreover, a number of recent results suggest smaller oligomeric aggregates, rather than the much larger amyloid fibrils, are critical in the pathogenesis.[10] However, the pathways of oligomerization and aggregation, as well as the nature of the oligomers and the relationships between the various aggregate structures, are poorly understood.

Models for PrP^{Sc} aggregation often presume that aggregates form through a classical nucleation and growth process,[5,11–14] possibly involving amplification of nuclei through fragmentation,[15,16] which leads to secondary nucleation. In the nucleation and growth model, as in all homogeneous nucleation models, initial aggregation of monomers is unfavored due to an increase in free energy associated with creation of small clusters. Yet once a cluster reaches the critical nucleus size, the change in free energy associated with further cluster growth becomes negative, and it can spontaneously grow to detectable size by subsequent monomer attachment. The idea that a nucleated growth model described PrP^{Sc} prion aggregation emerged from measurements of fibril aggregation kinetics during in vitro experiments[17–20] with recombinant cellular prion proteins ($rPrP^C$), which exhibited a lag phase of hours[19] even at concentrations much higher than in vivo PrP^C concentrations.[20] Moreover, this lag phase was reduced or disappeared at sufficiently high concentrations and upon seeding.[11] Recent research suggests that fibril fragmentation, which leads to secondary nucleation, can be a key process controlling the length of the lag phase and rate of aggregation, which still proceeds by monomer addition.[16]

One key aspect of prion aggregation not easily reconciled with the nucleation models is the formation of the so-called "*β*-oligomers", or "critical oligomers".[17,20–23] These are the most representative *β*-sheet-rich isoforms produced during in vitro experiments with $rPrP^C$. They are octameric or larger and were shown by Fourier-transform infrared (FTIR) spectroscopy

to have an extended antiparallel β-sheet structure.[21] However, they do not exhibit a lag phase.[21–23] Highlighting their importance, recent studies found that oligomers of PrP^{Sc} are the most toxic of prion particles.[24] Despite their significance, the formation pathway of β-oligomers has never been directly observed, the role of nucleation in their creation is unclear, and their connection to larger aggregates remains unknown.[25]

To address this lack of knowledge about β-oligomer formation pathways and to resolve the role of nucleation in both their creation and subsequent aggregate formation, we have developed a novel approach to tracking oligomerization using atomic force microscopy (AFM) that circumvents typical limitations on lateral resolution. We have used this approach to investigate the formation pathways of β-oligomers and subsequent nonfibrillar aggregates in three versions of full-length recombinant human prion proteins in which the number of repeats of an eight amino acid region, commonly referred to as the "octapeptide repeat region (ORR)", has been varied (see Supporting Information Figure S1A for location and extent of the ORR of human prion proteins).[23,26–30] These versions include the wild-type, which has 5 octapeptide repeats, and two pathogenic insertion mutants having 8 and 10 octapeptide repeats, respectively. We designate these three versions WT (MW: 22.8 KDa), 8OR (MW: 25.2 KDa), and 10OR (MW: 26.8 KDa).

We chose this insertion mutation for three reasons. First, clinical studies have shown that the onset and duration of familiar prion disease are inversely related to the number of additional ORR insertions; patients with more ORR insertions exhibit earlier onset of disease and shorter duration.[29] Second, recent studies have identified a number of potential mechanisms by which the ORR expansion might lead to earlier onset of disease. For example, a change in copper binding mode to the ORR may enhance redox stress or conversion to PrP^{Sc}.[30] Thus, this choice of mutation may confer clinical relevance to our observations of oligomerization and aggregation processes. Third, because this mutation allows us to vary the number of repeats systematically, it has the potential to provide us with mechanistic insights into its role in aggregation.

In terms of general relevance of these insertion mutants to other pathogenic prion proteins, such as point mutants with a mutation in just a single amino acid, many do share certain common conformational features, suggesting that they may also share common pathogenic mechanisms.[31]

However, whether or not our findings with insertion mutants are applicable to point mutants will require additional studies. Nonetheless, the insertion mutants provide a logical starting point, and the results presented below reveal a novel formation pathway for both the β-oligomers and the subsequent nonfibrillar aggregates and provide some insight into the possible mechanism by which insertion mutations may cause familiar prion disease.

EXPERIMENTAL SECTION

Experimental Materials

We used bacterially produced recombinant wild-type full-length human prion protein (WT) (sequence: 23–231) and two insertion mutant prion proteins (8OR and 10OR), which contain

three and five additional octapeptide (PHGGGWGQ) repeats, respectively.[23,28] (For generation and purification, see ref 28.) Bovine serum albumin (BSA) ≥96%, lyophilized powder, MW ∼66 KDa was obtained from Sigma (A4503-10G). Immunoglobulin G (IgG) (∼150 KDa) from human serum (56834-25MG) and Apo-ferritin (∼481.2 KDa) from equine spleen (A3641-100MG) were obtained from Sigma-Aldrich. Stock mycocerosic acid synthase (MAS) (∼224 KDa) was used.

Conversion of the Native r-Helix-Rich Conformation of rPrP^C into the β-Sheet-Rich Structure and Subsequent Aggregation

Transformation from the native R-helix-rich conformation of rPrP^C into the β-sheet-rich structure was induced by adding guanidine hydrochloride (GdnHCl) containing acidic buffer to rPrP^C solutions[18,22,23] (see Figure S2 for circular dichroism (CD) data showing structure change from α-helix-rich into the β-sheet-rich structure). Conditions of the experiments were based on Frankenfield et al.:[22] 100 μL of rPrP^C (40 μM) suspended in 50 mM NaOAc, 150 mM NaCl (pH 4) and 100 μL of 1 M GdnHCl, 50 mM NaOAc, 150 mM NaCl (pH 4) were preincubated at 37°C for 30 min. Next, 100 μL of GdnHCl buffer was introduced into 100 μL of rPrP^C solution to initiate aggregation. Thus, a 200 μL solution of 20 μM (final concentration) rPrP^C in 0.5 M (final concentration) GdnHCl, 50 mM NaOAc, 150 mM NaCl at pH = ∼4 was made. Samples not imaged immediately after mixing ($t = 0^+$ min) were incubated for first 30 min under rotation at 500 rpm. Incubation for the following 16.5 h was done at 0 rpm.

AFM Imaging

All imaging was done in tapping mode using a Nanoscope IIIA AFM (Digital Instruments, Santa Barbara, CA) equipped with a J scanner. For imaging in the air, silicon tips (type: FM) from Nanoworld with a typical tip radius of curvature less than 10 nm, force constant of 2.8 N/m, and resonance frequency of 75 kHz were used. For imaging in solution (in situ) environment, silicon nitride tips (type: OTR4) from Veeco Probes with a tip radius of ∼15 nm, force constant of 0.08 N/m, and resonance frequency of 34 kHz were used. When the silicon nitride tips were used to image proteins in the solution environment, the typical resonance frequency was around 7 kHz. All in situ imaging was performed in a commercial fluid cell.

For imaging 10OR in the nondenatured monomeric state (Figure 1A and B), 20 μL of 100 μM 10OR in 20 mM NaOAc (pH 5.5) was suspended in 80 μL of 20 mM NaOAc (pH 4.6) to get 20 μM 10OR in 20 mM NaOAc (pH ∼4.6). To obtain in situ images, a 45 μL aliquot was deposited on mica, and imaging was then carried out in the fluid cell. For ex situ imaging, 10 μL aliquot was deposited on mica for 4 min, rinsed with Milli-Q water, and dried with nitrogen gas prior to imaging. To prepare and image monomers of BSA, IgG, MAS, and apoferritin, a similar approach was used. For details, see Figures S4–S7.

For imaging newly formed 10OR oligomers at $t = 0^+$ min in the solution environment (Figure 1C, about 1 min after preparing 200 μL of solution with partially denaturing conditions as described above), 15 μL was deposited on mica, which was secured to the AFM scanner. Next, 30 μL of pure buffer (50 mM NaOAc, 150 mM NaCl (pH4)) was added

to the 15 μL solution. In situ imaging was then carried out. Because the reaction slowed drastically with time, we were able to observe oligomers formed for about 1 min as the signal stabilized enough to allow imaging. Thus, we could effectively observe the majority of particles that attached to the mica as soon as the 15 μL solution was deposited. For ex situ images (Figure 1D), another 200 μL of solution with the same composition was made. Within about 1 min after mixing, a 10 μL aliquot was deposited on mica for 4 min, rinsed with Milli-Q water, and dried with nitrogen gas prior to imaging.

Deterimination of Protein Particle Heights

Protein heights were obtained by analyzing height profiles from images such as those shown in Figure 1A–D using standard Veeco Nanoscope image analysis software.

RESULTS

Determining Protein Particle Size

Typically, AFM tip convolution effects prevent accurate measurement of lateral dimensions below about 10 nm (see Figure S1, B–H). During early stages of aggregation, which are the most important for probing underlying mechanisms, oligomers and/or aggregates should contain small numbers of monomers, which are below the discriminatory power of the conventional approach. Therefore, we developed a technique for estimating the size of protein particles smaller than the diameter of an AFM tip. Because AFM height measurements do not suffer from tip convolution effects and are accurate to ∼1 Å, we found that for globular proteins, we could obtain good size estimates of both oligomers and individual monomers adsorbed on mica by measuring their heights. However, because there was some distortion caused by interaction with the mica surface, we established a calibration curve using a strategy adopted from gel electrophoresis where marker proteins are used to estimate the mass of unknown proteins and protein fragments.

Using 10OR (MW: 26.8 KDa, Figure 1A and B) in the nondenatured monomeric state, bovine serum albumin (BSA, MW: ∼66 KDa, Figure S4), immunoglobulin G (IgG, MW: ∼150 KDa, Figure S5), mycocerosic acid synthase (MAS, MW: ∼224 KDa, Figure S6), and apoferritin (MW: ∼481.2 KDa, Figure S7) as five marker proteins, we constructed calibration curves from AFM height measurements for both in situ and ex situ conditions (Figure 2). As Figure 2 shows, over the investigated range of ∼25–150 kDa, these curves correlate well with the known dependence of hydrodynamic diameter on molecular weight. Thus, they allow us to use height measurements to directly estimate these quantities for globular proteins of unknown weight in the range of our calibration.

Formation of the Smallest Oligomeric Units

We used the calibration curves (Figure 2) to estimate the size of oligomers and aggregates formed from WT and 10OR following addition of guanidine hydrochloride (GdnHCl) containing acidic buffer. We found that WT and 10OR share a common, multistage pathway for β-oligomer and subsequent nonfibrillar aggregate formation, which is characterized by oligomers with well-defined sizes. Prior to aggregation ($t = 0^{-}$ min), WT and 10OR proteins existed in the original buffer (20 μM $rPrP^{C}$, 20 mM NaOAc, pH 5.5) mostly as monomers

with heights of around 1.5 nm ex situ and 2–3 nm in situ (Figure 3A–C). As soon as the GdnHCl containing acidic buffer was introduced ($t = 0^+$ min), small oligomers began to form with highly uniform heights in the range of ∼2–3 nm ex situ and ∼4.5–5.5 nm in situ (Figure 3D–F). From the calibration curves in Figure 2, we concluded that these were most likely trimers or possibly tetramers (molecular weights are WT trimer, 68.4 KDa; 10OR trimer, 80.4 KDa; WT tetramer, 91.2 KDa; 10OR tetramer, 107.2 KDa).

We suggest that these trimers and/or tetramers represent what have been interpreted in other studies as the nuclei for prion aggregation.[13,22] Although the oligomers must have overcome the energy barrier associated with entropy loss[13,37] due to oligomerization, which occurs when substantially unfolded monomers[38] from initially α-helix-rich conformation oligomerize into the β-sheet-rich structure, these oligomers are not nuclei as defined in the classical sense. Their smallest stable oligomer size that leads to further growth does not depend on concentration (i.e., supersaturation), and, as we show below, they do not undergo further growth by subsequent monomer attachment. Consequently, although these are equivalent to the smallest stable oligomers often assumed and referred to as nuclei in previous literature,[5,11–14,22] we will refer to them as seeds or growth units to avoid the term nuclei and still make a connection to the language of the cooperative polymerization model[39] described below.

This first result is consistent with and provides insight into a number of other experimental studies addressing prion kinetics, structure, and infectivity at both macroscopic and molecular scales. As we will show, analysis of previous turbidity studies indicates a monomer number of 3–4 in the smallest stable particles for both WT and 10OR aggregates (see Discussion and Figure S8 for details). Electron microscopy studies on 2D crystals of truncated PrP^{Sc} ($PrP^{Sc27–30}$) formed during the in vitro purification of infected tissues revealed a trimeric assembly of $PrP^{Sc27–30}$ as the basic unit.[9,40] Another study suggested that the smallest form of infectious PrP^{Sc} contains three or less prion protein monomers.[8] These results all correlate well with our observation of trimeric or tetrameric particles as the smallest stable unit of the β-sheet form of $rPrP^{C}$.

Growth of β-Oligomers and Nonfibrillar Aggregates

In addition to these rapidly formed basic units, immediately after introduction of GdnHCl-containing acidic buffer, larger oligomers, termed β-oligomers, started to form in both WT and 10OR solutions (Figure 1D, red arrow) and increased in number at longer incubation times (Figure 3J and K, red arrows). Circular dichroism (CD) measurements show that oligomerization is accompanied by a change from native R-helix-rich to β-sheet-rich structure (see Figure S2). These β-oligomers have ex situ heights mostly in the range of ∼5 to ∼7 nm. According to our calibration curve, this corresponds to particles containing ∼11–22 monomers, or ∼3–7 seeds. This second observation is also consistent with previous investigations. In a recent study, the most infectious PrP^{Sc} particles were found to contain about 14–28 prion protein monomers,[24] corresponding to about 4–9 of the basic growth units described here.

Surprisingly, β-oligomers did not form through addition of monomers to seeds. Rather, as documented in the series of images in Figure 4A–E and demonstrated by the decrease in

seed number with time in Figure 5, they were created primarily by direct interaction and coalescence of these basic growth units. This conclusion is consistent with that of Sokolowski et al.[21] based on FTIR measurements. Yet at this $rPrP^C$ concentration (20 μM), β-oligomers rarely grew beyond ~3–7 growth units in size. As Figure 4F and G demonstrates, all larger particles were loose aggregates of these β-oligomers. Note that the aggregates in Figure 4F and G are higher resolution images of the particles within the yellow boxes in Figure 3F and L, respectively. Figure 4H and I shows sequential in situ images documenting growth of β-oligomers and aggregates by particle addition, showing that this process occurs both in solution and on mica surfaces.

The nonfibrillar aggregates shown in Figure 4 are typical of all aggregates formed in our experiments, whereas many previous studies have reported the characteristic fibrillar form of prion aggregation. There are two primary reasons for the difference: (1) We have used full-length recombinant prion proteins in this study, which have only rarely been reported to form fibrils in vitro.[19,20] Previous studies suggest that full length PrP^{Sc} does not polymerize into fibrils in vitro because the N-terminal portion sterically inhibits stacking into the fibril form.[40] In contrast, most studies have investigated truncated versions.[17–20] Although these can easily form fibrils under mildly acidic conditions with moderate additions of denaturants such GdnHCl and Urea, they no longer contain the N-terminal portion, which includes the ORR. (2) The solution conditions used here are more conducive to facilitating the transformation to β-sheet-rich oligomeric forms, whereas fibrils generally form in less acidic conditions.[17,20]

This result further highlights the utility of this AFM-based approach to probing aggregate formation. As Figure 4 shows, the β-oligomers are closely spaced within the aggregates. Attempts to determine hydrodynamic diameters of protein aggregates using more common light scattering methods cannot give a true representation of aggregate structure because they will not resolve individual oligomers. In this situation, AFM imaging with the calibration curve of Figure 2 is far more useful because it provides the approximate hydrodynamic diameters of individual oligomers comprising the aggregates.

To summarize, the pathway to nonfibrillar aggregates is as follows: Upon partial denaturation, monomers (Figure 4A) combine to form trimeric or tetrameric seeds (Figure 4B). Subsequent growth does not follow a growth model in which monomers continue attaching to the seeds to form larger particles.[5,11–16] Instead, these basic growth units collide (Figure 4C) and coalesce to create the β-oligomers (Figure 4E). Figure 4C shows the moment just before three seeds coalesced into one β-oligomer (Figure 4E). This event was rarely observed, indicating that the kinetics of this process is rapid. A range of β-oligomer sizes are then created depending on how many growth units coalesce. However, nearly all of the β-oligomers are comprised of approximately 11–22 monomeric units, or ~3 to 7 seeds, regardless of incubation time. These results suggest that their size is thermodynamically limited, perhaps by strain[41] induced when a number of seeds coalesce into one larger oligomer. Subsequently, these β-oligomers cluster together to form nonfibrillar structures (Figure 4F), which then directly associate to form the largest aggregates (Figure 4G). Thus, as shown schematically in Figure 4J, the formation pathways of the β-oligomers and subsequent nonfibrillar aggregates for both WT and 10OR pass through multiple stages,

each of which is characterized by oligomers of a limited size range that give rise to the next stage through direct interaction and coalescence.

These results, combined with the previous study of Sokolowski et al.,[21] indicate that although prion replication in vivo has been considered to be concurrent with monomer attachment to aggregates based on many in vitro studies of prion fibril growth,[11,19] prion oligomers and aggregates may form via an oligomerization route that is subsequent to prion replication.

The Kinetics of Oligomerization and Aggregation

Although WT and 10OR exhibited similar pathways for non-fibrillar aggregate formation, the kinetics of monomer oligomerization and subsequent β-oligomer formation and aggregation differed significantly. As Figure 5A shows, upon initiation of oligmerization, 10OR produced a greater number of seeds than did WT, indicating that the additional five ORR in 10OR increased the probability for 10OR to transform from its native α-helix-rich into the β-sheet-rich structure[18,22,23] (see Figure S2 for CD data). After incubation at 37°C for 30 min, larger numbers of seeds, β-oligomers, and aggregates were observed in both samples, but the total number was still greater for 10OR (Figure 5A and B). Comparing the average number of seeds formed between $t = 0^+$ and 30 min, we obtained a seed formation rate for 10OR that was about 3 times larger than that for WT. In addition, 10OR produced larger nonfibrillar aggregates than did WT at both 30 min and 17 h (see Figure 3I and L for 10OR and Figure 3M for WT).

Interestingly, by 17 h, the number of seeds and β-oligomers that remained unincorporated into aggregates for 10OR was less than or equal to that for WT, with the rate of decrease in seed number having been 7 times greater for 10OR (Figure 5A). We presume that this is because the larger numbers of seeds at earlier times led to higher collision rates and thus a greater rate of seed coalescence and β-oligomer aggregation. With seed production having ceased, these higher rates led to a more rapid decrease in total number. Another series of experiments with 8OR, a recombinant mutant human prion protein containing three additional ORR insertions, exhibited aggregate sizes (Figure 3L–N) and an aggregation rate[23] between those observed for WT and 10OR. Moreover, a recombinant prion protein, $rPrP^{\Delta OR}$, that completely lacked the ORR produced a much slower aggregation rate than did WT as seen by optical turbidity under similar conditions.[42] These results show that oligomerization rates and resulting aggregate sizes increase as the number of octapeptide repeat motifs increases.

DISCUSSION

Seed Size

In the cooperative polymerization model of aggregation,[39] to obtain an analytical solution, one assumes: (1) there is a seed precursor one monomer shorter than the seed size that is in equilibrium with the monomer population throughout the reaction (pre-equilibrium); and (2) the polymer concentration changes only by irreversible seed formation (irreversibility). These assumptions do not depend on whether the seed is a nucleus in the classical sense

where its size depends on concentration, or merely a stable oligomer of fixed size that serves as the source of further aggregate growth.[39]

In this model, when the ratio of the total to equilibrium monomer concentration (α_T/α_e) $\gg$ 1, the delay, or relaxation, time (τ_D), defined as the time it takes the monomer concentration to reach some arbitrary fraction of its original value, scales with total initial monomer concentration (α_T) and seed size (n) through the following relationship:

$$\tau_D \propto \alpha_T^{-n/2} \quad (1)$$

Thus, (d log τ_D)/(d log α_T) = −(n/2) is obtained. In optical measurements[14,22] such as turbidity or fluorescence, this relationship is often used to obtain an approximate seed size by taking τ_D as the time to reach some arbitrary fraction of maximum optical signal for a range of α_T. (Although the turbidity signal is mainly influenced by aggregates larger than the trimeric/tetrameric seeds, because these aggregates arise from coalescence of the seeds, the signal can be quantitatively related to the consumption rate of monomers and used to obtain an approximate seed size through the equations that describe aggregate formation. The utility of this approach is demonstrated by Frankenfield et al.[22] who showed that analyses done by using data from three different assays, thioflavin T (ThT) fluorescence, monomer disappearance by gel filtration, and turbidity, all predict the same trimer or tetramer seed size.)

Strictly speaking, when eq 1 is used in experiments on rPrP aggregation to obtain n, the original meaning of monomers and α_T needs to be modified. In the kinetic equations of the cooperative polymerization model, the monomer is the species that incorporates into the polymer phase and α_T is the initial concentration of that monomer. However, when we use eq 1 to obtain the seed size from experiments in which aggregation is induced by a structural change from the initial R-helix-rich rPrP^C, the monomer is now the structure-altered protein, which is incorporated into the β-sheet aggregate phase. Similarly, α_T is the total concentration of the structure-altered protein (α'_T). Taking α'_T to be closely proportional to the initial R-helix-rich rPrP^C concentration (α_0) (i.e., $\alpha'_T \approx k\alpha_0$), the delay time becomes:

$$\tau_D \propto \alpha'^{-n/2}_T = (k\alpha_0)^{-n/2} \quad (2)$$

and n can still be obtained from the slope of log τ_D versus log α_0 (Figure S8).

Analysis of optical turbidity for both WT and 10OR shows that eq 2 is indeed obeyed. Using the cooperative polymerization model to estimate the seed size, one obtains n = 3–4 monomeric units (for details, see Figure S8). This is precisely the size of the smallest stable oligomers that we observed by AFM and that was proposed by others.[9,13,22,40] (See the caption to Figure S8 in the Supporting Information for an explanation of why both the pre-equilibrium and the irreversibility conditions are satisfied for the rPrP system in this study.) We note that our AFM and turbidity results together with those of a previous study[22] dealing with in vitro nonfibrillar aggregation of recombinant prion proteins suggest that, although the linear relationship between log τ_D and log α_0 can give an approximate seed size when

the system satisfies conditions of pre-equilibrium and irreversibility, it does not imply that further growth occurs by monomer attachment to the seeds.

Differences in Oligomerization and Aggregation Rates between WT and 10OR

In partially denaturing acidic conditions, monomers and β-oligomers exist in equilibrium.[38] However, because α-helix-rich monomers convert to structure-altered monomers before aggregation, we must assume that this equilibrium population of monomers consists of both α-helix-rich and structure-altered monomers, even though the concentration of the latter should be small as compared to that of the α-helix-rich monomers, given their strong tendency to oligomerize. This picture of rPrP aggregation in the presence of GdnHCl is identical to that of deoxyhemoglobin-S aggregation in the presence of carbon monoxide (see Figure S10).[43] Within this picture, the distinct differences in the oligomerization and aggregation rates between WT and 10OR can be explained using an empirical equation previously derived from deoxyhemoglobin-S aggregation, relating the rate of protein aggregation to the supersaturation ratio S (here $S = \alpha_T/\alpha_e$ where α_T is total initial protein concentration and α_e is the equilibrium solubility, i.e., the monomer concentration in equilibrium with aggregates when the reaction has reached equilibrium).[43] The relationship between S and the delay time (t_d (length of lag phase) or $t_{1/2}$ (time to reach half-maximum of optical signal)) is given by refs 43,44:

$$1/t_d = 1/t_{1/2} = \gamma S^n \quad (3)$$

where $1/t_d$ (=$1/t_{1/2}$) is a measure of the aggregation rate, γ is a constant, and n is the number of monomers in the seed.

On the basis of the AFM results for both WT and 10OR, the number of monomers in a seed is the same, that is, n = 3 or 4. Therefore, according to eq 3, the supersaturation ratio becomes the determining factor for the aggregation rates of both WT and 10OR. Because α_T for WT and 10OR and the temperature of the experiments were equal (α_T = 20 μM, T = 37°C), α_e was the only factor controlling the difference in aggregation rates. From previously published turbidity assays on 20 μM recombinant human prion proteins,[23] we obtain $t_{1/2}$ = 680 s for WT and $t_{1/2}$ = 75 s for 10OR (see Figure S8). Using eq 3 with n = 3, this implies that the equilibrium solubility for WT is 2.1 times greater than that of 10OR. If equilibrium truly exists between α-helix-rich monomers and β-oligomers in partially denaturing acidic conditions,[38] this same solubility ratio should also be obtained for different initial concentrations. Indeed, for a total initial concentration of 30 μM rPrP^C, the turbidity assay gave $t_{1/2}$ = 375 s for WT and $t_{1/2}$ = 35 s for 10OR, leading to a ratio of the WT to 10OR equilibrium solubility equal to 2.2, which is nearly identical to the ratio obtained at 20 μM.

These results imply that the fundamental reason insertion mutants exhibit both a greater rate of oligomerization and larger size aggregates is that they have a lower solubility in GdnHCl-containing acidic buffer (from eq 3, with n = 3, when WT has ∼2-fold larger solubility, 10OR has ∼8-fold larger initial aggregation rate). Because solubility is directly related to the free energy difference between the dissolved and condensed states, we propose that the presence of additional ORR units reduces the thermodynamic stability of the native α-helix-

rich structure relative to the β-sheet-rich structure in the destabilizing conditions created by GdnHCl-containing acidic buffer, thus leading to higher rates of oligomerization and aggregation. Yet in all cases, the mechanisms and pathways leading to aggregate formation remain the same.

Examining the biostatistics of human prion diseases, Stevens et al.[30] found a strong correlation between the number of ORR insertions and the onset age and duration of the familial prion disease. (See also Croes et al.[29]) Their analysis shows that the average onset age for the disease decreases from above 60 years with up to four additional ORR insertions to between about 30 and 40 years with five to nine additional insertions. They also found that this relationship was well correlated with results of their experiments on copper binding to ORR domains, showing that the copper binding properties of the ORR region suddenly change to a mode that may lead to enhanced redox stress or conversion to PrP^{Sc} with four or five additional ORR insertions. This dependence can also be correlated with the degree and kinetics of aggregation. As shown in the previously published turbidity assays (Figure 2D of ref 23), the aggregation kinetics increased dramatically when the number of additional ORR insertions was increased from three (8OR) to five (10OR) as compared to the case when it changed from zero (WT) to three ORR insertions (8OR). Using eq 3 with $n = 3$, we obtain a ratio of the WT to 8OR solubilities of 1.2 and 1.3 for protein concentrations of 20 and 30 μM, respectively ($t_{1/2}$ for 8OR = 408 s at 20 μM and 187 s at 30 μM (Figure 2B of ref 23)). Comparing this to the ratio of the WT to 10OR solubilities of 2.1 and 2.2 obtained above, we see that the scaling of solubility with ORR insertion number derived from our analysis mirrors the Stevens et al.[30] results on copper binding and onset of disease.

All studies with recombinant prion proteins produced in bacteria suffer from a lack of post-translational modifications and other cellular factors.[3,9] Recombinant prion protein aggregates (i.e., fibrils and β-oligomers) have not proven to produce serially transmissible prion diseases clearly when inoculated into animals.[4,17] However, the β-oligomers shown here do exhibit many of the physicochemical properties associated with PrP^{Sc} in that they have high β-sheet content and are relatively resistant to proteinase-K digestion.[4,17] Thus, although the primary significance of the current findings is that they elucidate the formation pathways of β-oligomers and their aggregates, they also suggest that the pathways to large oligomeric aggregates seen here may serve as a model for PrP^{Sc} oligomer formation in vivo, just as fibril formation by recombinant prion proteins observed in vitro has been taken as a model for PrP^{Sc} fibril formation in vivo.[17,19,20] Moreover, our findings linking oligomerization and aggregation kinetics to the number of ORR insertions correlate well with both the results from Stevens et al.'s[30] experiments on copper binding to ORR domains and the biostatistics of prion diseases in humans.[30] These correlations suggest that naturally occurring insertion mutants may also have lower thermodynamic stability as reflected through their solubility in vivo under destabilizing conditions, such as those created in our study by GdnHCl-containing acidic buffer. This would increase their susceptibility to conversion to PrP^{Sc} leading to oligomerization followed by formation of aggregates, which are the hallmark of prion diseases.

Supplementary Material

Refer to Web version on PubMed Central for supplementary material.

Acknowledgments

We thank Brent W. Segelke for providing mycocerosic acid synthase and Nicholas Fischer, Selim Elhadj, Dongbo Wang, and Youn-hi Woo for helpful discussions. This work was supported by Department of Defense National Prion Research Program (JJD DAMD17-03-1-0776; MSS DAMD17-03-1-286) and Lawrence Scholar Program Student Fellowship from Lawrence Livermore National Laboratory. K.R.C. acknowledges initial support from Graduate Study Abroad Scholarship by the Korean Science and Engineering Foundation (KOSEF). Y.H. acknowledges support from UCLA start-up funds and HSSEAS fellowship. This work was performed under the auspices of the U.S. Department of Energy by Lawrence Livermore National Laboratory under Contract DE-AC52-07NA27344 and at the Molecular Foundry, Lawrence Berkeley National Laboratory, with support from the Office of Science, Office of Basic Energy Sciences, of the U.S. Department of Energy under Contract No. DE-AC02-05CH11231.

References

1. Lansbury PT, Lashuel HA. Nature. 2006; 443:774–779. [PubMed: 17051203]
2. Maraganore DM, et al. J Am Med Assoc. 2006; 296:661–670.
3. Prusiner SB. Proc Natl Acad Sci USA. 1998; 95:13363–13383. [PubMed: 9811807]
4. Caughey B, Lansbury PT Jr. Annu Rev Neurosci. 2003; 26:267–298. [PubMed: 12704221]
5. Lee LY-L. J Am Chem Soc. 2007; 129:1644–1652. [PubMed: 17243682]
6. Pan K-M, Baldwin M, Nguyen J, Gasset M, Serban A, Groth D, Mehlhorn I, Huang Z, Fletterick RJ, Cohen FE. Proc Natl Acad Sci USA. 1993; 90:10962–10966. [PubMed: 7902575]
7. Chesebro B, Trifilo M, Race R, Meade-White K, Teng C, LaCasse R, Raymond L, Favara C, Baron G, Priola S, Caughey B, Masliah E, Oldstone M. Science. 2005; 308:1435–1439. [PubMed: 15933194]
8. Prusiner SB, Mckinley MP, Bowman KA, Bolton DC, Bendheim PE, Groth DF, Glenner GG. Cell. 1983; 35:349–358. [PubMed: 6418385]
9. Wille H, Michelitsch MD, Guenebaut V, Supattapone S, Serban A, Cohen FE, Agard DA, Prusiner SB. Proc Natl Acad Sci USA. 2002; 99:3563–3568. [PubMed: 11891310]
10. Brundin P, Melki R, Kopito R. Nat Rev Mol Cell Biol. 2010; 11:301–307. [PubMed: 20308987]
11. Jarrett JT, Lansbury PT Jr. Cell. 1993; 73:1055–1058. [PubMed: 8513491]
12. Come JH, Lansbury PT Jr. J Am Chem Soc. 1994; 116:4109–4110.
13. Nelson R, Sawaya MR, Balbirnie M, Madsen AØ, Riekel C, Grothe R, Eisenberg D. Nature. 2005; 435:773–778. [PubMed: 15944695]
14. Tobacman LS, Korn ED. J Biol Chem. 1983; 258:3207–3214. [PubMed: 6826559]
15. Wegner A, Savko P. Biochemistry. 1982; 21:1909–1913. [PubMed: 6805509]
16. Knowles TPJ, Waudby CA, Devlin GL, Cohen SIA, Aguzzi A, Vendruscolo M, Terentjev EM, Welland ME, Dobson CM. Science. 2009; 326:1533–1537. [PubMed: 20007899]
17. Baskakov IV, Legname G, Baldwin MA, Prusiner SB, Cohen FE. J Biol Chem. 2002; 277:21140–21148. [PubMed: 11912192]
18. Swietnicki W, Morillas M, Chen SG, Gambetti P, Surewicz WK. Biochemistry. 2000; 39:424–431. [PubMed: 10631004]
19. Baskakov IV, Bocharova OV. Biochemistry. 2005; 44:2339–2348. [PubMed: 15709746]
20. Bocharova OV, Breydo L, Parfenov AS, Salnikov VV, Baskakov IV. J Mol Biol. 2005; 346:645–659. [PubMed: 15670611]
21. Sokolowski F, Modler AJ, Masuch R, Zirwer D, Baier M, Lutsch S, Moss DA, Gast K, Naumann D. J Biol Chem. 2003; 278:40481–40492. [PubMed: 12917432]
22. Frankenfield KN, Powers ET, Kelly JW. Protein Sci. 2005; 14:2154–2166. [PubMed: 16046631]

23. Yu S, Yin S, Li C, Wong P, Chang B, Xiao F, Kang S-C, Yan H, Xiao G, Tien P, Sy M-S. Biochem J. 2007; 403:343–351. [PubMed: 17187581]
24. Silveira JR, Raymond GJ, Hughson AG, Race RE, Sim VL, Hayes SF, Caughey B. Nature. 2005; 437:257–261. [PubMed: 16148934]
25. Amorphous protein aggregates have been studied by others. See, for example:Lundberg, et al. Chem Biol. 1997; 4:345–355. However, they typically represent a preamyloid stage as described in the work of:Lomakin; et al. *Proc. Natl. Acad. Sci. U.S.A.* 1996, 93, 1125–1129. They are on the pathway to true amyloids. Most importantly, they have structure similar to that of the unstructured monomers and are a transient state that dissociates while forming amyloids. This is in contrast to the *β*-oligomers, which already have *β*-sheet-rich structure and are not on the pathway to amyloid fibril formation but, rather, form larger, amorphous aggregates: Baskakov; et al. *J. Biol. Chem.* **2002**, 277, 21140–21148. [PubMed: 9195875]
26. Zahn R. J Mol Biol. 2003; 334:477–488. [PubMed: 14623188]
27. Chattopadhyay M, Walter ED, Newell DJ, Jackson PJ, Aronoff-Spencer E, Peisach J, Gerfen GJ, Bennett B, Antholine WE, Millhauser GL. J Am Chem Soc. 2005; 127:12647–12656. [PubMed: 16144413]
28. Yin S, Yu S, Li C, Wong P, Chang B, Xiao F, Kang S-C, Yan H, Xiao G, Grassi J, Tien P, Sy M-S. J Biol Chem. 2006; 281:10698–10705. [PubMed: 16478730]
29. Croes EA, Theuns J, Houwing-Duistermaat JJ, Dermaut B, Sleegers K, Roks G, Van den Broeck M, van Harten B, van Swieten JC, Cruts M, Van Broeckhoven C, van Duijin CM. J Neurol Neurosurg Psychiatry. 2004; 75:1166–1170. [PubMed: 15258222]
30. Stevens DJ, Walter ED, Rodríguez A, Draper D, Davies P, Brown DR, Millhauser GL. PLoS Pathog. 2009; 5:1–11.
31. Yin S, Pham N, Yu S, Li C, Wong P, Chang B, Kang S-C, Biasini E, Tien P, Harris DA, Sy M-S. Proc Natl Acad Sci USA. 2007; 104:7546–7551. [PubMed: 17456603]
32. Manelyte L, Urbanke C, Giron-Monzon L, Friedhoff P. Nucleic Acids Res. 2006; 34:5270–5279. [PubMed: 17012287]
33. Maiti NR, Surewicz WK. J Biol Chem. 2001; 276:2427–2431. [PubMed: 11069909]
34. Wilkins DK, Grimshaw SB, Receveur V, Dobson CM, Jones JA, Smith L. J Biochemistry. 1999; 38:16424–16431.
35. Rosenqvist E, JØssang T, Feder J. Mol Immunol. 1987; 24:495–501. [PubMed: 3657792]
36. Petsev DN, Thomas BR, Yau ST, Vekilov PG. Biophys J. 2000; 78:2060–2069. [PubMed: 10733984]
37. Chothia C, Janin J. Nature. 1975; 256:705–708. [PubMed: 1153006]
38. Baskakov IV, Legname G, Prusiner SB, Cohen FE. J Biol Chem. 2001; 276:19687–19690. [PubMed: 11306559]
39. Goldstein RF, Stryer L. Biophys J. 1986; 50:583–599. [PubMed: 3779001]
40. Govaerts C, Wille H, Prusiner SB, Cohen FE. Proc Natl Acad Sci USA. 2004; 101:8342–8347. [PubMed: 15155909]
41. Aggeli A, Nyrkova IA, Bell M, Harding R, Carrick L, McLeish TCB, Semenov AN, Boden N. Proc Natl Acad Sci USA. 2001; 98:11857–11862. [PubMed: 11592996]
42. Yu S, Yin S, Pham N, Wong P, Kang SC, Petersen RB, Li C, Sy MS. FEBS J. 2008; 275:5564–5575. [PubMed: 18959744]
43. Hofrichter J, Ross PD, Eaton WA. Proc Natl Acad Sci USA. 1976; 73:3035–3039. [PubMed: 9640]
44. Kodaka M. Biophys Chem. 2004; 109:325–332. [PubMed: 15110949]

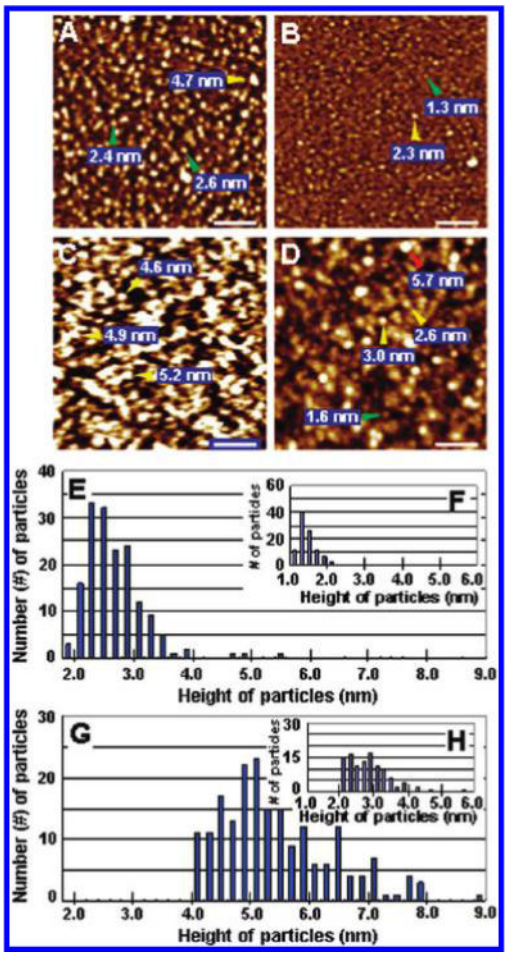

Figure 1.

AFM images of 10OR monomers and oligomers. (A) In situ and (B) ex situ images of 10OR in native state. (C) In situ and (D) ex situ images of 10OR immediately after preparation of partially denaturing solution (at $t = 0^+$ min). Numbers next to arrowheads in (A)–(D) give heights of adjacent protein particles where green = monomers, yellow = oligomers, and red = β-oligomer. (E–H) Height distributions of (E,F) 10OR in native state and (G,H) newly formed 10OR oligomers at $t = 0^+$ min, where (E,G) are from in situ images and (F,H) are from ex situ images. For the complete height distribution of 10OR including monomers at $t = 0^+$ min at ex situ condition, see Figure S3. Scale bars, 100 nm.

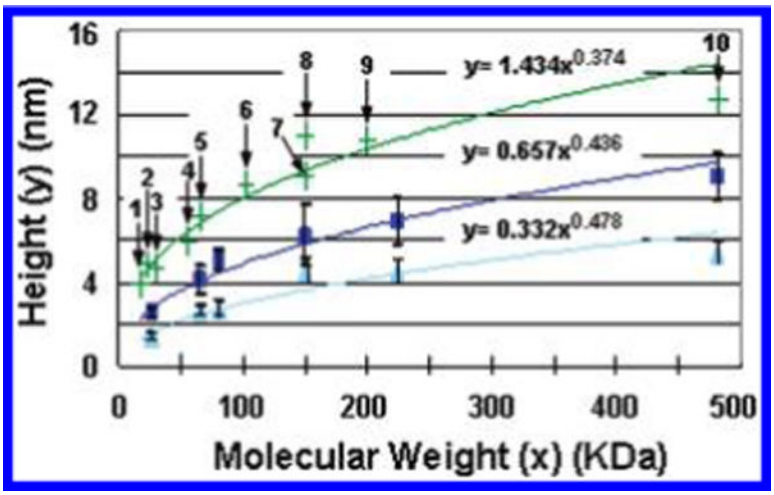

Figure 2.

Heights of marker proteins and newly formed 10OR oligomers (at $t = 0^+$ min) deposited on mica versus molecular weights. Heights were measured from the surface of mica to the top of protein particles. Light blue ▲: ex situ curve where, from left to right, points are for 10OR monomers (26.8 KDa), BSA monomers (∼66 KDa), majority of newly formed 10OR oligomers (seeds) such as those marked with yellow arrowheads in Figure 1, C and D assuming they are trimers (80.4 KDa), IgG monomers (∼150 KDa), MAS monomers (∼224 KDa), and Apoferritin monomers (∼481.2 KDa). Dark blue ■: in situ curve where order left to right is the same as for ex situ curve. Green +: hydrodynamic diameters. Numbers indicate: 1, myoglobin monomer (16.9 KDa);[32] 2, WT monomer (22.8 KDa);[33] 3, carbonic anhydrase monomer (29 KDa);[32] 4, yeast triosephosphate isomerase dimer (∼56 KDa);[34] 5, BSA monomer;[32] 6, hexokinase monomer (102 KDa) (Malvern Instruments); 7, alcohol dehydrogenase dimer (150 KDa);[32] 8, IgG monomer;[35] 9, *β*-amylase monomer (200 KDa);[32] 10, apoferritin monomer.[36] Error bars represent ±one standard deviation.

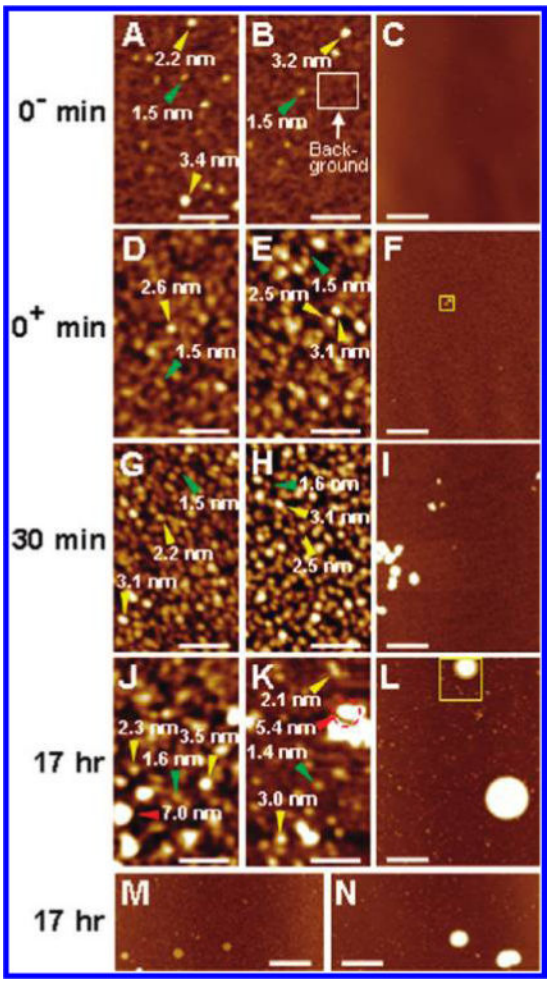

Figure 3.

The formation of oligomers and nonfibrillar aggregates. (A–L) Ex situ images of WT and 10OR before (A–C) and after (D–L) mixing with partially denaturing buffer. For solution preparation conditions, see the Experimental Section. (A) WT and (B,C) 10OR in original buffer. (D) WT and (E,F) 10OR at $t = 0^+$ min. (G) WT and (H,I) 10OR at t = 30 min. (J) WT and (K,L) 10OR at t = 17 h. (M,N) Ex situ images of WT (M) and 8OR (N) at t = 17 h after mixing partially denaturing buffer. Numbers next to arrowheads are heights of adjacent particles with color coding as in Figure 1. Scale bars are 100 nm for (A,B, D,E,G,H,J,K) and 2 μm for (C,F,I,L,M,N).

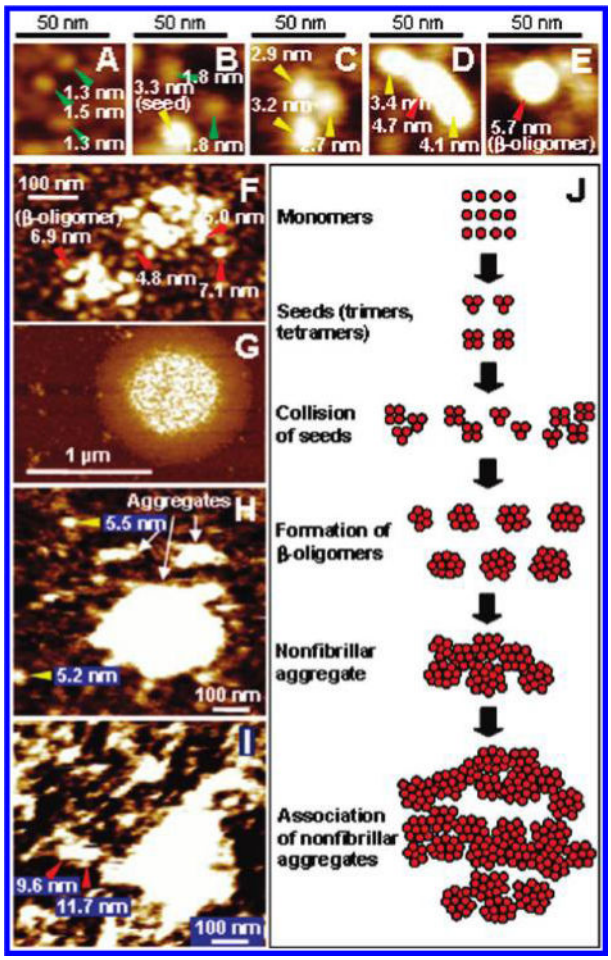

Figure 4.

Pathway leading to formation of *β*-oligomers and subsequent nonfibrillar aggregates. (A–G) Ex situ images of 10OR showing (A) monomers; (B) monomers and a small oligomer (seed); (C) collision of seeds at the moment just before coalescence into one *β*-oligomer; (D) interaction of a seed with two oligomers; (E) a *β*-oligomer; (F) nonfibrillar aggregates at early stage of formation showing that they are comprised of *β*-oligomers (higher resolution image of yellow rectangle in Figure 3F); and (G) large aggregate formed by direct association of small, irregular nonfibrillar aggregates like those in (F) (higher resolution image of yellow rectangle in Figure 3L). (H and I) Sequential in situ images captured in the same spot on mica showing small oligomers (seeds) and aggregates composed of *β*-oligomers. Following collection of (H), freshly mixed 10OR solution (partially denaturing) was added, and image (I) was collected. It shows growth of the aggregates in (H) as well as a newly formed aggregate composed of two *β*-oligomers with heights 9.6 and 11.7 nm. For solution preparation conditions, see the Experimental Section. (See also Figure S9 for details.) (J) Schematic of observed pathway to formation of *β*-oligomers and subsequent nonfibrillar aggregates illustrating multiple stages of association by stable oligomeric intermediates.

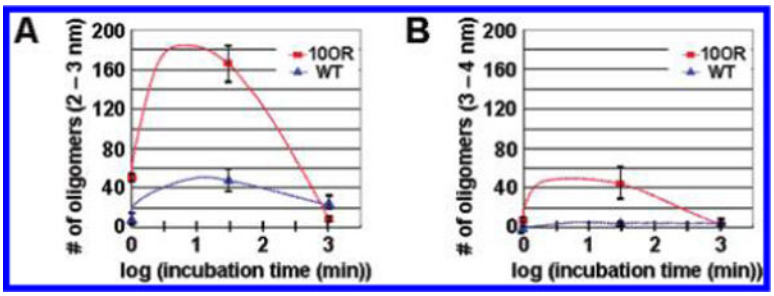

Figure 5.

Kinetics of oligomerization. (A,B) Number of oligomers with heights between (A) 2–3 nm and (B) 3–4 nm versus incubation time. Red, 10OR; blue, WT.